

Achieving High-Performance Perovskite Photovoltaic by Morphology Engineering of Low-Temperature Processed Zn-Doped TiO₂ Electron Transport Layer

Ming-Chung Wu,* Yen-Tung Lin, Shih-Hsuan Chen, Meng-Huan Jao, Yin-Hsuan Chang, Kun-Mu Lee, Chao-Sung Lai, Yang-Fang Chen, and Wei-Fang Su

Perovskite solar cells (PSCs) have become one of the most promising renewable energy converting devices. However, in order to reach a sufficiently high power conversion efficiency (PCE), the PSCs typically require a high-temperature sintering process to prepare mesostructured TiO₂ as an efficient electron transport layer (ETL), which prohibits the PSCs from commercialization in the future. This work investigates a low-temperature synthesis of TiO₂ nanocrystals and introduces a two-fluid spray coating process to produce a nanostructured ETL for the following deposition of perovskite layer. The temperature during the whole deposition process can be maintained under 150 °C. Compared to the typical planar TiO₂ layer, the perovskite layer fabricated on a nanostructured TiO₂ layer shows uniform compactness, preferred orientation, and high crystallinity, leading to reproducible and promising device performance. The detail mechanisms are revealed by the contact angle test, morphology characterization, grazing incident wide angle X-Ray scattering measurement, and space charge limited currents analysis. Finally, optimized device performance can be achieved through adequate Zn doping in the TiO₂ layer, demonstrating an average PCE of 19.87% with champion PCE of 21.36%. The efficiency can maintain over 80% of its original value after 3000 h storage in ambient atmosphere. This study suggests a promising approach to offer high-efficiency PSCs using the low-temperature process.

1. Introduction


Energy crisis raised the necessity for the development of renewable energy, which opens opportunities for solar energy. There is enormous solar energy for solar cells to harvest and solve energy problems. Perovskite solar cells (PSCs) have grown potentially due to their remarkable photovoltaic performance and economical cost. Therefore, it has become a hot research topic in recent years.^[1–6] Currently, PSC achieved a record high power conversion efficiency (PCE) of 25.2% in 2019. According to the order of selective carrier contacts, the PSCs can be divided into two main categories: n-i-p and p-i-n structures.^[7–11] The architecture of n-i-p structure is the electron transport layer (ETL)/absorber layer/hole transport layer (HTL), and the p-i-n architecture is in the reversed order. The n-i-p configuration has a lot of processing advantages compared to p-i-n structure, such as resistance to humidity which can effectively prevent the degradation of the PSCs and prolong its

Prof. M.-C. Wu, Y.-T. Lin, S.-H. Chen, Y.-H. Chang, Prof. K.-M. Lee
Department of Chemical and Materials Engineering
Chang Gung University
Taoyuan 33302, Taiwan
E-mail: mingchungwu@cgu.edu.tw

Prof. M.-C. Wu, Dr. M.-H. Jao, Prof. K.-M. Lee, Prof. C.-S. Lai
Green Technology Research Center
Chang Gung University
Taoyuan 33302, Taiwan

Prof. M.-C. Wu, Prof. K.-M. Lee
Division of Pediatric Neonatology
Department of Pediatrics
Chang Gung Memorial Hospital
Linkou, Taoyuan 33305, Taiwan

Prof. C.-S. Lai
Department of Electronic Engineering
Chang Gung University
Taoyuan 33302, Taiwan

 The ORCID identification number(s) for the author(s) of this article can be found under <https://doi.org/10.1002/smll.202002201>.

Prof. C.-S. Lai
Department of Nephrology
Chang Gung Memorial Hospital
Linkou, Taoyuan 33305, Taiwan

Prof. C.-S. Lai
Department of Materials Engineering
Ming Chi University of Technology
New Taipei City 24301, Taiwan

Prof. Y.-F. Chen
Department of Physics
National Taiwan University
Taipei 10617, Taiwan

Prof. W.-F. Su
Department of Materials Science and Engineering
National Taiwan University
Taipei 10617, Taiwan

Prof. W.-F. Su
Advanced Research Center for Green Materials Science and Technology
National Taiwan University
Taipei 10617, Taiwan

DOI: 10.1002/smll.202002201

stability.^[12–13] N-type materials (e.g., TiO₂, ZnO, SnO₂) as ETL is suitable for PSC due to their appropriate band alignment with perovskite absorber.^[14–16] For example, mesoporous TiO₂ as ETL has achieved an impressive cell efficiency. The mesoporous scaffold offered a short charge carrier transport distance. Therefore, the extraction efficiency of the ETL could be considerably increased. However, the high crystallinity for such structure relying on the high-temperature sintering process (450–550 °C), which limits the development of flexible PSC and further impedes the large-scale application of such device. Pursuing an alternative process (i.e., low-temperature process) to reduce the energy required in the fabricating process is imperative.

The PSCs based on various low-temperature ETL has been reported to obtain high photovoltaic performance. Snaith et al. introduced a facile method, using ZnO to prepare a low-temperature ETL and achieved a high PCE of 21.1%. The ZnO solution was prepared by dissolving the ZnO powder in ammonia hydroxide and water, followed by spin-coating the ZnO solution and annealing at 120 °C.^[17] A TiO₂ blocking underlayer has been developed by Grätzel et al. using an anodic electrodeposition method.^[18] Thin Ti^{IV}-based films were fabricated from TiCl₃ aqueous precursors in an electrochemical cell at room temperature. After a sintering process at 150 °C, the TiO₂ blocking underlayer was successfully prepared and achieved a PCE of 14%. Recently, Im et al. synthesized TiO₂ nano-sol for ETL by sol–gel reaction at acidic aqueous phase.^[19] The procedure of low-temperature-processed PSCs was carried out at the temperature below 100 °C and achieved a PCE of 18.2% and 15.8% for rigid and flexible solar cells, respectively. Taking the advantages of these advances, the low-temperature process with much lower heating demands (<150 °C) increases the possibility of flexible PSC and opens the door to mass-production.

However, all those reported low-temperature processes can only obtain planar structure ETL. It has been mentioned that the mesostructured ETL can facilitate the extraction of electron.^[20–25] Besides, the texture of substrate can significantly influence the crystallization process of perovskite layer during deposition. S. Liu group has declared that perovskite layer with increased crystallinity and surface coverage can be achieved via controlling the wettability between perovskite droplet and the substrate.^[26] In another work from S. Wang group, a substrate containing a 3D framework was introduced to modify the interaction with perovskite droplet.^[27] After the modification, the perovskite layer exhibiting better surface coverage and reduced pinhole can be obtained, resulting in enhanced device performance.

In this report, we developed a strategy using a low-temperature solution process to prepare the nanostructured substrate for efficient PSCs. We synthesized highly crystalline TiO₂ nanocrystals and presented a two-fluid spray coating route to prepare high-quality TiO₂ ETL. By controlling the deposition parameters during spray coating, nanostructured TiO₂ ETL with desired morphology was obtained. The perovskite layer fabricated on top of the nanostructured TiO₂ ETL showed higher crystallinity, preferred orientation and better surface coverage compared to the one deposited on planar TiO₂ ETL. The increased quality of perovskite layer remarkably enhanced the device performance. Besides, the band structure and electrical properties were carefully tuned by doping Zn into TiO₂

ETL.^[28,29] Not only did it facilitate the transport of electrons, but it also enhanced the charge mobility after doping metal ion. Finally, the optimized PSCs achieved a high average PCE of 19.87%, with the champion device showing a PCE of 21.36%. We believe this facile, economic, and efficient strategy in PSCs offers a promising opportunity for the large-scale production and commercialization of PSCs in the future.

2. Results and Discussion

2.1. Low-Temperature TiO₂ Nanocrystals Characterization

Low-temperature TiO₂ (LT-TiO₂) nanocrystals (NCs) were synthesized via a non-hydrolytic sol–gel method^[30] and all procedures were operated in ambient air. Two key conditions controlling the quality of ETL are the crystallinity of LT-TiO₂ NCs and the dispersity of LT-TiO₂ NCs colloidal solution. Highly crystalline LT-TiO₂ NCs suppress the number of trap states and ensure the efficient extraction of electrons. The good dispersity of LT-TiO₂ NCs colloidal solution enables the reproducible film deposition process and produces a compact and uniform thin film. We examined the crystallinity of LT-TiO₂ NCs through XRD measurement. **Figure 1a** shows the XRD pattern, which indicates our LT-TiO₂ NCs crystallize into anatase phase with a space group of body-centered tetragonal (JCPDS Card no. 21–1272). The crystal size of anatase LT-TiO₂ NCs was confirmed by transmission electron microscopy (TEM), and the size was about 4 nm in diameter (**Figure 1b**). From TEM images, a clear lattice fringe could be observed, implying the high crystallinity of our LT-TiO₂ NCs. In terms of dispersity, we first dispersed our LT-TiO₂ NCs in ethanol. The dispersion of NCs in solution has a great impact on the uniformity of film formation. If the LT-TiO₂ NCs agglomerate in the solution, it could lead to films containing macroscale agglomerates and further result in poor photovoltaic performance. Therefore, a small amount of titanium diisopropoxide bis(acetylacetonate) (Ti(acac)₂OiPr₂) was added into the precursor solution to improve the dispersity. The photograph of LT-TiO₂ NCs dispersed in ethanol is shown in **Figure 1c**, and the difference between the solutions is the presence of Ti(acac)₂OiPr₂. After adding Ti(acac)₂OiPr₂ into the solution, the precursor solution became translucent due to the chelation of acetylacetonate ligands to the LT-TiO₂ NCs.^[31] Besides, the solution can be kept stable without precipitation for 1 year. Ti(acac)₂OiPr₂ not only decomposed to TiO_x during the drying procedure but also bridged the gaps between the NCs. Ti(acac)₂OiPr₂ could be seen as electronic glue between the NCs in thin film, which resulted in the enhanced conductivity and thus efficiently enhanced the operation of solar cells.

2.2. LT-TiO₂ Film Deposition

The substrate for perovskite deposition plays a critical role. The interaction between substrate and perovskite precursor solution can significantly affect the growth of perovskite thin film. Many research groups dedicated to investigating the relationship between those two, and it was reported that a structured substrate can facilitate the growth of compact and continuous

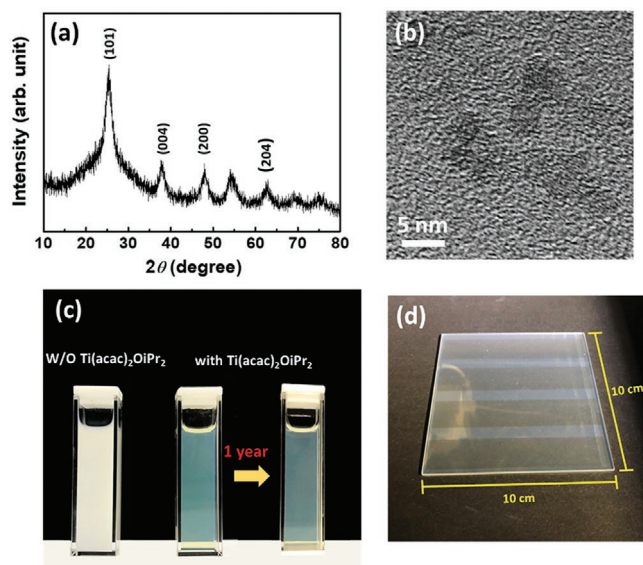


Figure 1. Characterization of LT-TiO₂ NCs. a) XRD pattern of LT-TiO₂ NCs, showing distinct diffraction peaks of anatase phase (JCPDS Card no. 21-1272). b) TEM images of LT-TiO₂ NCs, showing average diameter of 4 nm. c) Dispersion of LT-TiO₂ NCs in ethanol. The addition of Ti(acac)₂OiPr₂ can enhance the dispersity of LT-TiO₂ NCs in ethanol with colloidal stability over 1 year. d) Photographs showing LT-TiO₂ NCs deposited through two-fluid spray coating on 10 cm × 10 cm FTO glass.

perovskite thin film.^[20–25] Here in our research, we proposed a two-fluid spray coating technique, combined with volatile ink solution and preheated substrate (Figure S1, Supporting Information), to fabricate a structured ETL composed of LT-TiO₂ NCs.

The two-fluid spray coating method blended LT-TiO₂ NCs colloidal solution and high-pressure gas in the two-fluid nozzle, LT-TiO₂ NCs colloidal solution was carried out of the nozzle by the gas and sprayed on the substrate in the form of aerosol or mist. The highly volatile solvent of NCs colloidal solution and the elevated temperature of substrate accelerated the evaporation of solvent upon the landing of LT-TiO₂ NCs on the substrate, allowing a structure to be formed quickly. However, the

compact and uniform thin film could still be achieved after randomly and repeatedly spraying aerosol. By carefully tuning the concentration of colloidal ink, the flow rate of carrier gas, and the number of depositions, it was possible to deposit globally uniform thin film containing the desired local structure. Additionally, the two-fluid spray coating technique is readily scalable. As a proof of concept, we deposited a uniform LT-TiO₂ layer on a 100 cm² FTO substrate, as shown in Figure 1d. This large-scale solution-processable spray coating method can be seen as a promising technique for producing large-area PSCs.

We prepared LT-TiO₂ thin films by spin coating or spray coating with different gas flow rates. The topography was characterized using atomic force microscope (AFM). As shown in Figure 2, both depositing methods can produce a high surface coverage on the FTO glass. A smooth and dense LT-TiO₂ layer can be observed from the spin coating method (Figure 2a). On the other hand, for the spray coating method, there are some ring-like protruding nanostructures on the prepared thin film (Figure 2b–d). As a result, the surface roughness obtained by a spray coating method is much higher (RMS = 42.9, 92.1, and 157.6 nm, for Figure 2b–d, respectively) compared to that using a spin coating method (RMS = 27.2 nm). We believe the droplets of aerosol induced the ring-like protruding structures. Meanwhile, the height of protruding structures can be manipulated through the gas flow rate. The higher the gas flow rate, the smaller the aerosol would be, and resulting in smaller protruding structures.

2.3. Device Performance

We examined the performance of perovskite photovoltaics on different ETLs prepared from spin coating or spray coating strategy. The architecture of the device is FTO glass/LT-TiO₂/CH₃NH₃PbI_{3(1-x)}Br_{3x}/spiro-OMeTAD/Ag, where $x = 0.05$ for mixing halide perovskite. The photovoltaic parameters extracted from the $J-V$ curves are summarized based on 40 individual devices (Table 1). For spin coating method, the optimal thickness of LT-TiO₂ is determined to be 130 nm, and the average device PCE is 14.97% (Table S1, Supporting Information).

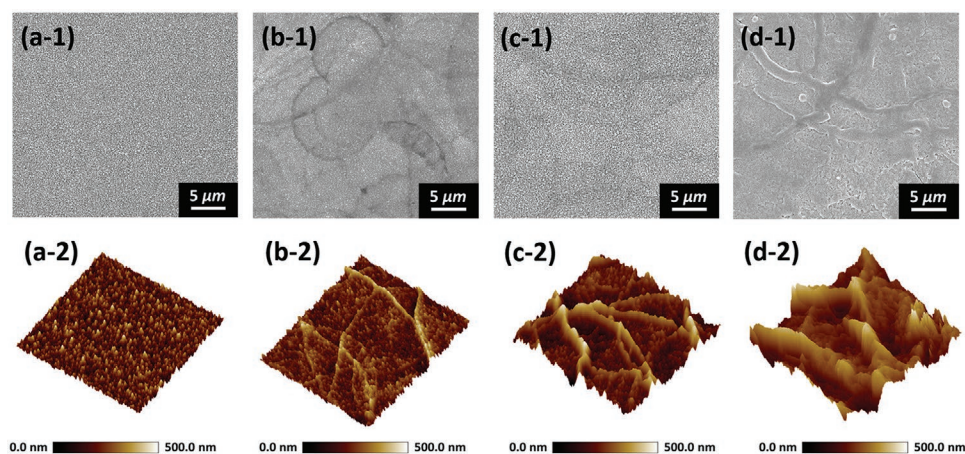


Figure 2. SEM images (upper section) and AFM topographies (lower section) showing the structure of LT-TiO₂ thin film deposited by different strategies. By a) spin coating, spray coating with carrier gas flow rate of b) 10 LPM (liters per minute), c) 5 LPM, or d) 2 LPM.

Table 1. Device performance of devices with LT-TiO₂ ETL based on spin coating and spray coating method.

ETL	V _{oc} [V]	J _{sc} [mA cm ⁻²]	FF [%]	PCE [%]
Spin	1.02 ± 0.02	21.64 ± 1.08	67.20 ± 6.76	14.97 ± 1.85
Spray 10 LPM ^{a)}	1.02 ± 0.02	21.08 ± 0.76	69.52 ± 2.42	14.91 ± 0.75
Spray 5 LPM	1.02 ± 0.01	22.27 ± 0.55	73.97 ± 1.89	16.95 ± 0.51
Spray 2 LPM	0.91 ± 0.01	8.58 ± 1.19	47.46 ± 1.75	3.71 ± 0.60

^{a)}LPM: Liters per minute.

On the other hand, the optimized performance for the spray method is 16.95% with the best PCE of 17.80%. For spray LT-TiO₂ ETL, the height of protruding nanostructure is found as an essential factor controlling the device performance. If the dimension of protruding nanostructure is more significant than that of the perovskite layer, undesired carrier recombination will occur during carrier transporting due to the possible contact of the opposite carrier transport layers. On the contrary, ETL that is insufficiently thick will lead to reduced extraction ability of electrons and excessive interface defects. Therefore, when operating the two-fluid spray coating process, we deliberately controlled the flow rate of carrier gas to manipulate the dimension of ETL nanostructures. When the thickness of LT-TiO₂ of both processes was optimized, the LT-TiO₂ ETL based on the spray method exhibited higher photovoltaic performance. Besides, we also observe that the standard deviation of efficiency is much smaller for spray coating-based devices than that of the spin coating-based devices. Therefore, we can infer that using a two-fluid spray technique to prepare LT-TiO₂ ETL is able to enhance the uniformity of as-fabricated devices. In the following sections, we will consider only the optimal fabricating processes and focus on the essential parts that differentiate spin and spray coating methods.

2.4. Perovskite Film Morphology

The major difference of LT-TiO₂ thin film between spin coating and spray coating is LT-TiO₂ film morphology. Considering the deposition of perovskite layer is sensitive to its substrate, we believed the improvement of photovoltaic performance can be attributed to the increased quality of perovskite thin films.^[20–25]

The morphology of the perovskite active layer deposited on the LT-TiO₂ ETL prepared by the different methods is shown in Figure 3a,d. The perovskite film deposited on spin LT-TiO₂ presents a high density of pinholes with a diameter of 50 nm. The existence of the pinholes could result in severe current leakage and reduce the FF of device. In contrast, a pinhole-free film was obtained from the perovskite layer deposited on LT-TiO₂ ETL using the spray coating method. We explicitly quantified the differences by calculating the pinhole ratio using image analysis program (Figure S3, Supporting Information). According to the analysis, the pinhole ratio of spin LT-TiO₂ based perovskite thin film is 1%, while that of spray LT-TiO₂ based perovskite thin film is only 0.07%. The significantly reduced pinhole ratio could be attributed to the hydrophilic surface of the spray TiO₂ ETL. The interface properties of the perovskite layer/LT-TiO₂ ETL were investigated by the static contact angles of deionized water

on LT-TiO₂. The static contact angles of water on the LT-TiO₂ decreased from 37.8° to 15.3° after changing from the spin-coating to the spray coating process (Figure 3b,e). The improved surface wettability of LT-TiO₂ can be described by Wenzel's model:

$$\cos\theta = r \times \cos\theta_e \quad (1)$$

where θ is an apparent contact angle, r is the roughness ratio, and θ_e is the contact angle corresponding to the ideal surface.^[32] The theory is based on the assumption that a rough surface extends the solid-liquid interface area in comparison to the projected smooth surface and consequently reduces the contact angle. Compared to spin coating method, the concentric rings created by spray coating provide a rough surface which dramatically enhances the surface wettability and suppresses the dewetting of the deposited perovskite films during thermal annealing. Therefore, perovskite thin film showing high crystallinity and limited pinholes could be fabricated.

To further probe the quality of perovskite layers grown on various substrates, we performed grazing incident wide angle X-ray scattering (GIWAXS) measurement using synchrotron radiation. The grazing incident setup assures the collected data comes from the entire device and is more representative of information for our samples (Figure 3c,f). From the obtained patterns, we found that the perovskite film deposited on spray LT-TiO₂ exhibited stronger diffraction signals than that on the spin LT-TiO₂, which can be clearly confirmed through 1D integration diagram (Figure S4, Supporting Information). The sharp and robust diffraction peak for the perovskite film based on spray LT-TiO₂ implies that the films possess good crystallization and large crystal size. One thing worth noting is that spray LT-TiO₂ will induce crystallization of (110) crystal plane along q_z direction (Figure 3g), indicating stronger preferred orientation. To further reveal the detail, we calculated the azimuthal intensity plot along the ring at q ≈ 10 nm⁻¹, which can be assigned to the (110) crystal plane for perovskite. The result is shown in Figure 3h. From the azimuthal plot, we found the orientation of perovskite thin film can be heavily influenced by the TiO₂ layer. The perovskite films grown on spin LT-TiO₂ showed that the formation of randomly oriented crystallites accompanied by a significant decrease of out-of-plane-oriented crystallites. On the contrary, the perovskite films based on spray LT-TiO₂ exhibited a sharp peak at 90° azimuth angle, indicating a large amount of preferential out-of-plane oriented crystallites. These crystallites can promote the carriers transporting at the grain boundaries. Therefore, we believe the protruding structured TiO₂ layer made by spray coating can increase the wetting behavior during the growth of perovskite, inducing a strongly oriented and highly crystalline perovskite thin film.

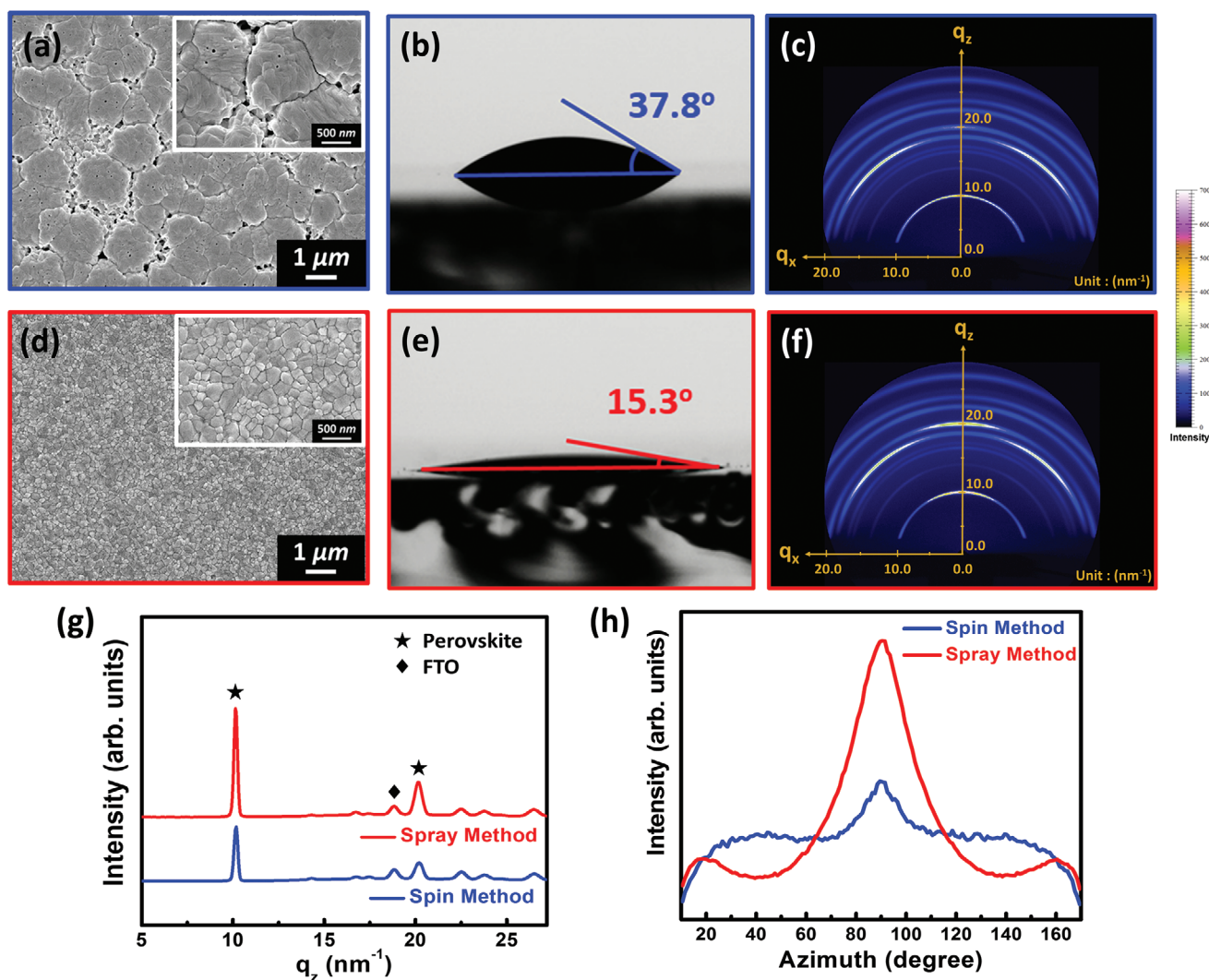


Figure 3. a,d) SEM images, b,e) contact angle measurements, and c,f) GIWAXS 2D patterns for perovskite layer fabricated on spin coated or spray coated LT-TiO₂ NCs, respectively. g) Line cut of GIWAXS 2D patterns at q_z direction. h) Azimuthal plot of GIWAXS 2D pattern at (110) crystal plane.

2.5. Device Characterization

In terms of photovoltaic performance, the increased crystallinity and preferred orientation are believed to suppress the recombination process of carriers during transporting. The charge recombination mechanism of perovskite device can be revealed by light intensity-dependent open-circuit voltage measurements.^[33] The relationship between V_{oc} versus light intensity is shown as follows:

$$V_{oc} = V_s + \frac{nk_B T}{q} \ln \frac{P}{P_s} \quad (2)$$

where V_{oc} is the open-circuit voltage at various light intensities, V_s is the open-voltage at 100 mW cm⁻², P represents various light intensities, P_s is the standard light intensity (100 mW cm⁻²), n is the ideal factor, k_B is the Boltzmann constant, T is the absolute temperature (298.15 K), and q is the elementary charge. Under the open circuit condition, the build-in

potential across the device is zero. As a consequence, the photo-generated carriers are prone to recombine. For ideal bimolecular recombination, the recombination rate is dependent only on the incident light intensity. Therefore, the ideal factor n is close to unity. However, if there are many trap states in a photovoltaic device, trap assisted Shockley-Read-Hall recombination prevails, and open-circuit voltage will heavily depend on the concentration of both types of carriers, making ideal factor close to 2. We examined the recombination mechanism of our devices by controlling the intensity of incident light from 1 sun illumination (100 mW cm⁻²) to 1 mW cm⁻². The result is shown in **Figure 4a,b**. As the illumination intensity decreased, the V_{oc} of the device based on spin LT-TiO₂ dropped faster than the one based on spray LT-TiO₂, which means that a higher proportion of trap assisted recombination occurred in spin LT-TiO₂ based device. This can be quantified by fitting the V_{oc} versus light intensity plot with the equation. For spin LT-TiO₂ based device, the derived ideal factor is equal to 2.09. On the contrary, the ideal factor for spray LT-TiO₂ based device comes to a much

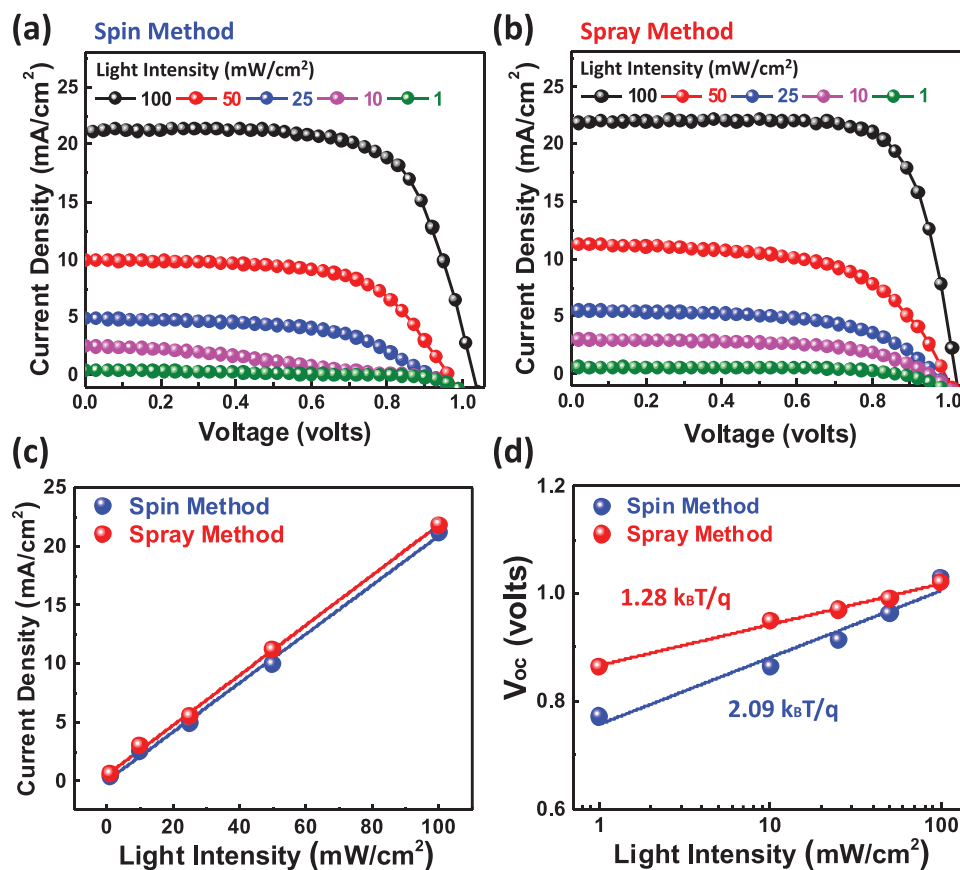


Figure 4. Light-intensity-dependent J - V characterization curves of perovskite photovoltaics based on a) spin LT-TiO₂ and b) spray LT-TiO₂ as ETL. c) Linear fitting of j_{sc} versus light intensity. d) Linear fitting of V_{oc} versus logarithmic light intensity.

smaller value of 1.28 (Figure 4d). It is a strong evidence that the perovskite crystalline thin films grown on spray LT-TiO₂ shows better quality than those grown on spin LT-TiO₂.

2.6. Large Area Cell

One of the advantages of the spray coating technique is the uniformity across the large area. Adding this advantage to the compact and pinhole-free perovskite layer achieved using spray LT-TiO₂, it encouraged us to fabricate devices with increased size. Hence, we fabricated various spin LT-TiO₂ and spray LT-TiO₂ photovoltaics with device areas ranging from 0.09, 0.25, 0.49, to 1.00 cm². The active areas versus PCE are shown in Figure 5a,b. When we increased the device area, the performance of spin LT-TiO₂ based PSC dropped dramatically, with efficiency of less than 5% on the 1.00 cm² device. On the contrary, the performance of spray LT-TiO₂ based PSC exhibited less impact from the enlarging device area, with averaged efficiency remaining over 12% on the 1.00 cm² device. Meanwhile, we measured PCE through probing at various positions of our 1.00 cm² device to confirm the uniformity of films (Figure 5c). If pinholes or traps were to present across the device, enlarging the active device area would increase the rate of carrier recombination and rapidly deteriorate the device performance. The

results not only confirm the homogeneity of spray LT-TiO₂ thin film but also verify the suppressed formation of pinholes in the perovskite layer grown on spray LT-TiO₂ thin film.

2.7. Zn Doping in LT-TiO₂

We have demonstrated the ability of nanostructured LT-TiO₂ compact layer prepared by a two-fluid spray technique inducing the growth of highly crystalline pinhole-free perovskite thin film and promoting the performance of perovskite photovoltaic. In order to further improve the efficiency of PSCs, we employed Zn doping into our LT-TiO₂ NCs. Metal ion doped in TiO₂ is an effective strategy to enhance the electrical conductivity and modulate the band levels. Many reports have been published to explain the influence and benefit of appropriate doping in TiO₂.^[34–39] In our early research, we also revealed that Zn-doped TiO₂ can significantly raise the electron extraction ability and align energy level well with perovskite.^[28,29] Accordingly, we chose Zn as a dopant and design synthesis route to obtain Zn:LT-TiO₂ NCs. We synthesized Zn:LT-TiO₂ NCs through the reaction of ZnCl₂, TiCl₄, and benzyl alcohol at 85 °C under ambient atmosphere (discussed in Supporting Information). Because the charge transfer kinetics and electron extraction behavior can be influenced by the doping ratio, we synthesized

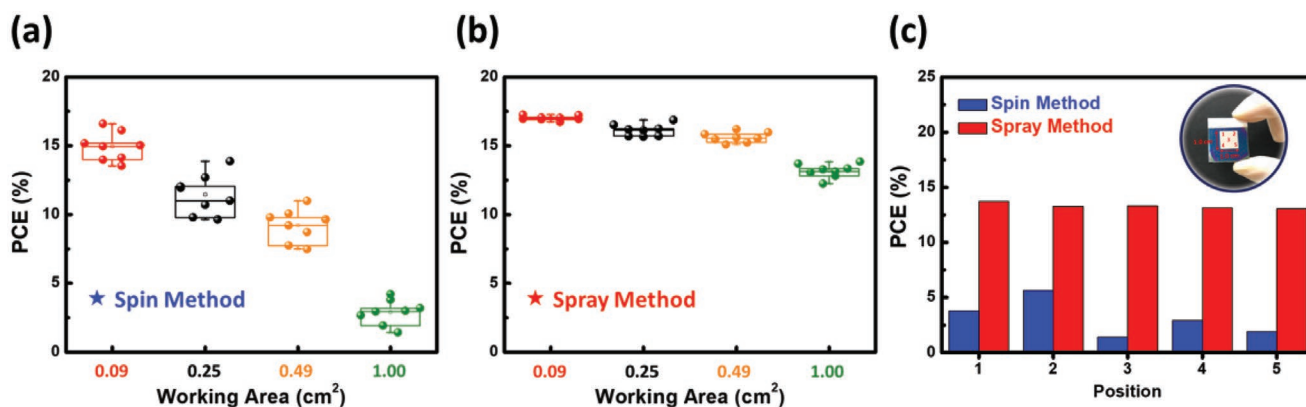


Figure 5. The area-dependent statistical performance for devices based on a) spin LT-TiO₂ and b) spray LT-TiO₂ as ETL. c) Efficiency of 1.00 cm² device probed at different spots.

a series of Zn:LT-TiO₂ NCs with various doping ratios and examined their XRD and performance (Figures S5 and S6, Supporting Information).

The result showed that the best performance of perovskite photovoltaics was achieved using 1.00 mol% Zn:LT-TiO₂ as ETL and spray coating deposition method. The averaged efficiency of 19.87% was achieved from 40 individual devices. With respect to the key parameters in *J*-*V* characteristic curves, the enhanced performance can be attributed to the simultaneous increase of *V*_{oc} and FF (see Table 2 and a summarized data in Table S2, Supporting Information).

The increase of *V*_{oc} can be the result of better energy level alignment between Zn:LT-TiO₂ and perovskite. Ultraviolet photoelectron spectroscopy (UPS) and absorption measurements were carried out to verify our hypothesis (Figures S7 and S8, Supporting Information). From the measurement, after doping 1.00 mol% Zn into the LT-TiO₂ NCs, the conduction band minimum was estimated to increase from -3.95 to -3.89 eV and the valence band maximum shifted from -7.37 to -7.25 eV. Ideally, there should be no electron barrier at the perovskite/Zn:LT-TiO₂ interface, which facilitates electron extraction. Besides, we can also observe the Fermi level increase to the higher binding energy. This result explained the remarkable *V*_{oc} increase after doping zinc ion into ETL. In addition to the interface between the perovskite/Zn:LT-TiO₂, the carrier transfer in the ETL is another crucial issue for PV performance. For this reason, we studied the electron transfer characteristic of various kinds of LT-TiO₂ thin films by space charge limited currents measurement.^[40,41] We fabricated FTO glass/LT-TiO₂/Au samples with non-doped LT-TiO₂ and Zn:LT-TiO₂. The trap density (*N*_t) can be determined by the equation:

$$V_{\text{TFL}} = \frac{eN_t d^2}{2\epsilon\epsilon_0} \quad (3)$$

Table 2. Device performance and key parameters of devices with non-doped or Zn-doped LT-TiO₂ based ETL.

ETL	<i>V</i> _{oc} [V]	<i>J</i> _{sc} [mA cm ⁻²]	FF [%]	PCE [%]	<i>R</i> _s [Ω cm ²]
Non-doped LT-TiO ₂	1.02 ± 0.01	22.27 ± 0.55	73.97 ± 1.89	16.95 ± 0.51	5.09 ± 1.10
Zn:LT-TiO ₂	1.11 ± 0.02	22.98 ± 0.50	78.15 ± 2.00	19.87 ± 0.69	3.48 ± 0.59

where *V*_{TFL} is trap-filled limit voltage, *e* is the elementary charge, *ε* is the relative dielectric constant of TiO₂, and *ε*₀ is the permittivity of free space. In Figure 6a, 1.00 mol% Zn:LT-TiO₂ exhibited a relative low trap-state density of 3.32 × 10¹⁶ cm⁻³. Obviously, we can suggest that doping Zn in LT-TiO₂ alleviates the trap states and mitigates non-radiative recombination. In ohmic region (Figure 6b), we can determine electrical conductivity using the following equation:

$$I = \sigma_0 (A/d)V \quad (4)$$

where *A*, *d*, and *σ*₀ are sample area, thickness, and electrical conductivity, respectively. The conductivity was estimated to increase from 2.18 × 10⁻³ to 8.07 × 10⁻³ mS cm⁻¹ after doping 1.00 mol% Zn into ETL. Furthermore, we can explore the carrier mobility (Figure 6c) using Mott-Gurney law:

$$J = \frac{9}{8} \mu \epsilon \epsilon_0 \frac{V^2}{d^3} \quad (5)$$

where *ε*₀ is the permittivity of free space and *ε* is the dielectric constant of TiO₂. Apparently, the electron mobility of 1.00 mol% Zn:LT-TiO₂ film came to about 1.41 × 10⁻⁴ (cm² Vs⁻¹), which was higher than that of non-doped LT-TiO₂ at 8.57 × 10⁻⁵ (cm² Vs⁻¹). These results demonstrated that Zn doping could effectively promote the carriers transport in ETL film and lower the series resistance in device (Table 2). As a consequence, the FF and PCE of device can be improved.

2.8. Device Stability

The overall structure of the device is FTO glass/Zn:LT-TiO₂/CH₃NH₃PbI_{3(1-x)}Br_{3x}/spiro-OMeTAD/Ag electrode with *x* = 0.05, the schematic diagram and SEM cross-section are shown in Figure 7a,b, respectively. The best performing device exhibited an efficiency of 21.36%, with key parameters extracted from *J*-*V* characteristic curve shown in Figure 7c. Another persuasive approach to check the device performance is through a stabilized PCE method. Therefore, we operated the champion device at its maximum output voltage and measured the

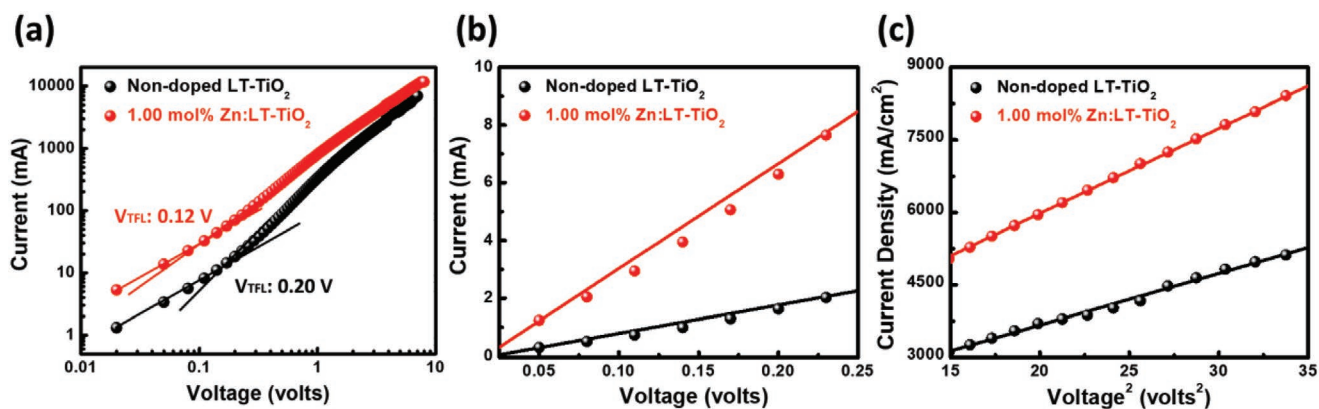


Figure 6. Electronic properties characterization of non-doped LT-TiO₂ and Zn:LT-TiO₂ ETLs. a) Trap filled limit voltage derived from space-charge-limited current measurement. b) Conductivity derived from ohmic region. c) Mobility derived using Mott-Gurney equation.

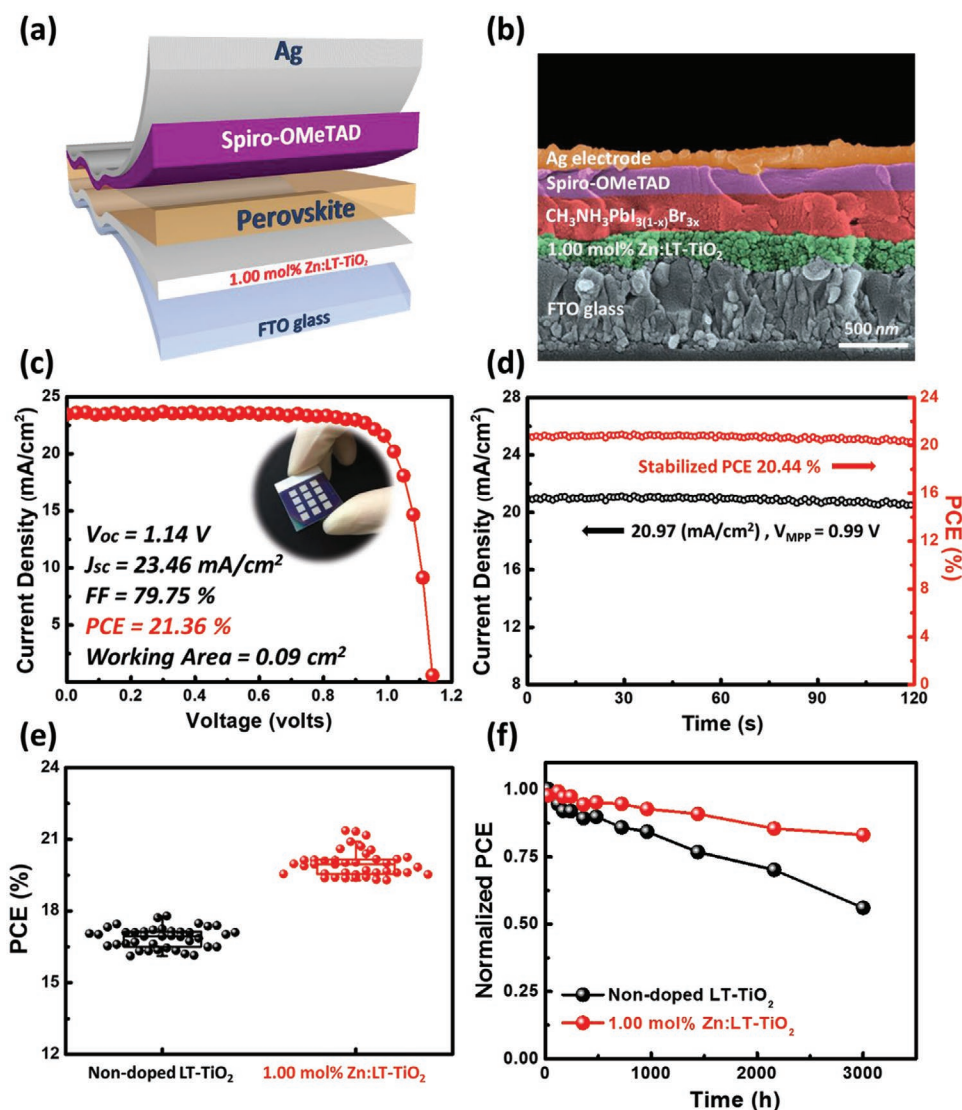


Figure 7. a) Schematic diagram of device structure. b) SEM cross-section of our device. c) J - V characterization and key parameters obtained from champion device. d) Current density and efficiency output of champion device when operated under 0.99 V. e) The statistical efficiency distribution of devices based on non-doped LT-TiO₂ and Zn:LT-TiO₂. f) Stability test of devices based on non-doped LT-TiO₂ and Zn:LT-TiO₂ under ambient condition.

current density to calculate PCE. When the device was biased at 0.99 V, an output current density of 20.97 mA cm⁻² could be measured (Figure 7d), suggesting an efficiency of 20.44%. The cross-validation using different characterization methods confirms the reliability of the efficiency of our device. It is worth noting that our result approaches the PCE of perovskite photovoltaics made based on meso-TiO₂, which requires the elevated-temperature energy-consuming sintering process. Figure 7e shows the efficiency distribution of two-fluid spray coated devices with non-doped LT-TiO₂ and Zn:LT-TiO₂ as ETL. The narrow efficiency distributions confirm the reproducibility and homogeneity of device achieved by spray coating strategy. In addition, the statistical results exhibit the superior performance obtained from Zn:LT-TiO₂ over non-doped LT-TiO₂. We examined the long-term stability of our devices after 3000 h (more than 4 months) of storage in ambient atmosphere (about 30% relative humidity, 25 °C) (Figure 7f). In previous studies, the long-term stability of PSCs can be affected by crystallinity, trap states at grain boundary, and charge accumulation between the ETL/perovskite interfaces during operation.^[42–44] The devices based on 1.00 mol% Zn:LT-TiO₂ could retain 83% of their original PCE, whereas those on non-doped LT-TiO₂ only retained 56% of their initial efficiency. The detailed statistics of V_{oc} , J_{sc} , and FF decays over time exhibited that the reduced J_{sc} and FF was the main reason for the PCE decrease (Figure S12, Supporting Information). The enhanced stability can be explained by the increased crystallinity of perovskite layer on Zn-doped TiO₂, which has been found in our previous study,^[28] as well as the superior charge extraction ability to suppress the interfacial recombination. These results confirm that Zn:LT-TiO₂ ETL prepared by spray coating method is a great ETL for high-performance and stable perovskite photovoltaics.

3. Conclusion

We provide a two-fluid spray coating technique with Zn:LT-TiO₂ NCs as ETL to fabricate high-performance perovskite photovoltaics under low processing temperature. A compact ETL containing nanostructure can be obtained using two-fluid spray coating technique. By controlling the deposition parameters in the spray coating process, thin-film morphology can be effectively modified. We found that perovskite layer deposited on various ETL will exhibit various morphologies and properties. The nanostructured ETL could induce the formation of uniform and compact perovskite thin film with preferred orientation, while planar ETL only resulted in random-oriented perovskite thin film with pinholes. As a consequence, spray coated LT-TiO₂ perovskite devices showed higher performance. To further enhance PCE, we improved the conductivity and band alignment using Zn:LT-TiO₂. An averaged efficiency of 19.87% with the champion device showing the efficiency of 21.36% could be achieved. It is worth noting that the temperature for the entire fabrication process can be maintained below 150 °C. Our report suggests a low-temperature large-scalable process to obtain high-performance perovskite photovoltaic, paving the way for future commercialization.

4. Experimental Section

Synthesis of Zn-Doped LT-TiO₂ (Zn:LT-TiO₂) Nanocrystals: LT-TiO₂ and Zn:LT-TiO₂ nanocrystals were synthesized by the non-hydrolytic sol-gel method. First, zinc chloride (99.99%, Acros Organics) was dissolved in 8 mL of anhydrous ethanol (≥99.8%, Sigma-Aldrich) with various stoichiometric ratios. Next, 2.0 mL TiCl₄ (99.9%, Acros Organics) was added dropwise to anhydrous ethanol in a beaker in ice bath. After returning to room temperature, 40.0 mL of anhydrous benzyl alcohol (99%, Acros Organics) was added to the previous solution and then heated to 85 °C for 12 h. Then, a translucent dispersion of Zn:LT-TiO₂ nanocrystals in the final solution was observed. Furthermore, the precipitate Zn:LT-TiO₂ was washed with diethyl ether and centrifuged at 8000 rpm for 20 min. After centrifugation, the Zn:LT-TiO₂ precipitate was dispersed in anhydrous ethanol and titanium diisopropoxide bis(acetylacetonate) (TiAcAc, 75 wt%, Sigma-Aldrich). Finally, the light yellow transparent solution can be obtained, which is stable without precipitation for over 12 months.

Preparation of Electron Transport Layer: The FTO glass (7Ω, FrontMaterials Co. Ltd.) was cleaned by deionized water, acetone, and isopropanol, followed by 10 min of UV-ozone treatment. To control the morphology of ETL, spin-coating method and spray-coating method were used to prepare the spin coating ETL and spray coating ETL, respectively. The schematic illustration of depositing the ETL by spin coating and spray coating on FTO glass are shown in Figure S1, Supporting Information. For spin coating method ETL, the LT-TiO₂ precursor solution was spin-coated on FTO substrates (2 × 2 cm²) at 1500 rpm for 30 s, followed by 30 min of thermal treatment at 150 °C in ambient air. For spray coating method ETL, the FTO substrate (10 × 10 cm²) was placed onto the heated stage at 150 °C during the spray coating process in ambient air. The spray coating machine from Long-Light Machinery Co. Ltd. was used in this study. The spray head movement rate of x-axis was 5 m min⁻¹ and the flow rate of LT-TiO₂ dispersion was 2 × 10⁻³ LPM. Furthermore, the flow rate of carrier gas (dry air) was 2 to 10 LPM. After spray coating process, the ETL was annealed at 150 °C for 30 min.

Fabrication of the Perovskite Solar Cells: The perovskite solution was prepared with lead iodide (PbI₂, 99.9985%, Alfa Aesar), methylammonium iodide (CH₃NH₃I, MAI, FrontMaterials), and methylammonium bromide (CH₃NH₃Br, MABr, Alfa Aesar) dissolved in a mixture solution of γ-butyrolactone (GBL, ≥99%, Sigma-Aldrich) and dimethyl sulfoxide (DMSO, 99.9%, ECHO) with a 1:1 volume ratio. The molar ratio of MAI:PbI₂:PbBr₂ was 1:0.95:0.05. The perovskite solution was coated onto the substrate with two steps spin coating procedure. First step was 1000 rpm for 10 s, and then the spinning speed was raised to 5000 rpm for 20 s. 100 μL of toluene was dropped on the perovskite layer during the second spin coating step at 17 s before the end of the procedure. After that, the perovskite layer was annealed at 100 °C for 10 min. The hole transport solution consisted of 80 mg 2,2',7,7'-Tetrakis[N,N-di(4-methoxyphenyl)amino]-9,9'-spirobifluorene (spiro-OMeTAD, FrontMaterials) in chlorobenzene. To it, 17.5 μL lithium bis(trifluoromethanesulfonyl)imide (Li-TFSI, 98+, Alfa Aesar) (104 mg mL⁻¹ in acetonitrile) was added, followed by 28.5 μL of 4-tert-butylpyridine (tBP, 98%, Sigma-Aldrich). The HTL was subsequently spin-coated at 2500 rpm for 30 s. Finally, 120 nm thick silver electrode was deposited on top of HTL via thermal evaporation.

Characterization of Materials and Devices: The crystal structure and microstructure of LT-TiO₂ ETL were analyzed by X-ray diffraction pattern (XRD, D2 phaser with Xflash 430, Bruker) and high-resolution transmission electron microscopy (spherical aberration-corrected ULTRA-HRTEM, JEM-ARM200FTH, JEOL), respectively. The surface morphology and roughness were characterized by field-emission scanning electron microscope (SU-8010, HITACHI) and AFM (Bruker Multimode2-U-NSV, Bruker), respectively. The hydrophilicity of ETLs was measured by water contact angle meter. The GIWAXS patterns were analyzed by synchrotron X-ray spectroscopy (λ ≈ 1.0256 Å) on beamline 13A1 of the National Synchrotron Radiation Research Center (NSRRC), Taiwan. The photoluminescence (PL) spectra of samples were measured by a continuous-wave diode laser beam (λ_{exc} = 440 nm, PDLH-440-25,

Dongwoo Optron Co. Ltd.). Time-resolved photoluminescence spectra were obtained by a time-correlated single-photon counting spectrometer (WELLS-001 FX, Dongwoo Optron Co. Ltd.). The absorption spectra were measured using a UV-vis spectrometer (V-730, Jasco). The UPS (Sigma Probe, Thermo VG-Scientific) measurements were conducted by Hel (21.2 eV) lamp.

The current–voltage (J – V) characteristics were measured by digital source meter (2400, Keithley) in ambient conditions under simulated solar illumination at 100 mW cm⁻², AM 1.5G standard. The light source was calibrated with a Si-reference cell (BS-520BK, Bunkokeiki, BS-520BK) with KG-5 filter. The reverse scan and forward scan J – V curves were measured from 1.2 to –0.1 V and –0.1 to 1.2 V, respectively. The step voltage was fixed at 10 mV, and the delay time was fixed at 200 ms. The external quantum efficiency (EQE) of device was characterized by EQE measurement system (QE-R, Enli Technology Co., Ltd). The impedance spectrum analysis was carried out by Solartron Analytical (Material Lab XM) instrument.

Supporting Information

Supporting Information is available from the Wiley Online Library or from the author.

Acknowledgements

M.-C. Wu, Y.-T. Lin and S.-H. Chen contributed equally to this work. The authors appreciate Dr. Ming-Tao Lee (BL-13A1) and Dr. Jyh-Fu Lee (BL-17C1) at National Synchrotron Radiation Research Centre for useful discussion and suggestions. Long-Light Machinery Co. Ltd. provides the equipment and valuable advice for spray coating process. The financial support from Ministry of Science and Technology, Taiwan (Project No. 106-2221-E-182-057-MY3, 108-2119-M-002-005, 109-2221-E-182-059, 109-2634-F-002-042, and 109-3116-F-002-001-CC2), Ministry of Education in Taiwan (ME 109L9006), Chang Gung University (QZRPD181) and Chang Gung Memorial Hospital, Linkou (CMRPD2H0173 and BMRPC74) are highly appreciated.

Conflict of Interest

The authors declare no conflict of interest.

Keywords

morphology, perovskites, solar cells, spray coating, TiO₂

Received: April 5, 2020

Revised: July 1, 2020

Published online: September 20, 2020

- [1] J. Burschka, N. Pellet, S.-J. Moon, R. Humphry-Baker, P. Gao, M. K. Nazeeruddin, M. Grätzel, *Nature* **2013**, 499, 316.
 [2] M. Liu, M. B. Johnston, H. J. Snaith, *Nature* **2013**, 501, 395.
 [3] D. Prochowicz, M. Sasaki, P. Yadav, M. Grätzel, J. Lewinski, *Acc. Chem. Res.* **2019**, 52, 3233.
 [4] P. Wang, Y. Wu, B. Cai, Q. Ma, X. Zheng, W.-H. Zhang, *Adv. Funct. Mater.* **2019**, 29, 1807661.
 [5] D. Li, L. Song, Y. Chen, W. Huang, *Adv. Sci.* **2019**, 7, 1901397.
 [6] Y. Cheng, F. So, S.-W. Tsang, *Mater. Horiz.* **2019**, 6, 1611.
 [7] Q. Lin, A. Armin, P. L. Burn, P. Meredith, *Acc. Chem. Res.* **2016**, 49, 545.
 [8] L. Meng, J. You, T.-F. Guo, Y. Yang, *Acc. Chem. Res.* **2016**, 49, 155.

- [9] S. Wang, T. Sakurai, W. Wen, Y. Qi, *Adv. Mater. Interfaces* **2018**, 5, 1800260.
 [10] H. Kim, K.-G. Lim, T.-W. Lee, *Energy Environ. Sci.* **2016**, 9, 12.
 [11] M. Habibi, F. Zabihi, M. R. Ahmadian-Yazdi, M. Eslamian, *Renewable Sustainable Energy Rev.* **2016**, 62, 1012.
 [12] F. Guo, X. Sun, B. Liu, Z. Yang, J. Wei, D. Xu, *Angew. Chem., Int. Ed.* **2019**, 58, 1.
 [13] N. Arora, M. I. Dar, A. Hinderhofer, N. Pellet, F. Schreiber, S. M. Zakeeruddin, M. Grätzel, *Science* **2017**, 358, 768.
 [14] Y. Yang, C. Liu, Y. Ding, Z. Arain, S. Wang, X. Liu, T. Hayat, A. Alsaedi, S. Dai, *ACS Appl. Mater. Interfaces* **2019**, 11, 34964.
 [15] G. Yang, H. Tao, P. Qin, W. Ke, G. Fang, *J. Mater. Chem. A* **2016**, 4, 3970.
 [16] Y. Zhou, X. Li, H. Lin, *Small* **2019**, 16, 1902579.
 [17] K. Schutt, P. K. Nayak, A. J. Ramadan, B. Wenger, Y.-H. Lin, H. J. Snaith, *Adv. Funct. Mater.* **2019**, 29, 1900466.
 [18] S. H. Aung, L. Zhao, K. Nonomura, T. Z. Oo, S. M. Zakeeruddin, N. Vlachopoulos, T. Sloboda, S. Svanstrom, U. B. Cappel, A. Hagfeldt, M. Grätzel, *J. Mater. Chem. A* **2019**, 7, 10729.
 [19] M. S. You, J. H. Heo, J. K. Park, S. H. Moon, B. J. Park, S. H. Im, *Sol. Energy Mater. Sol. Cells* **2019**, 194, 1.
 [20] C.-H. Chan, C.-R. Lin, M.-C. Liu, K.-M. Lee, Z.-J. Ji, B.-C. Huang, *Adv. Mater. Interfaces* **2018**, 5, 1801118.
 [21] H. Kim, J. Hong, C. Kim, E.-Y. Shin, M. Lee, Y.-Y. Noh, B. Park, I. Hwang, *J. Phys. Chem. C* **2018**, 122, 16630.
 [22] A. Gagliardi, A. Abate, *ACS Energy Lett.* **2018**, 3, 163.
 [23] K. Mantulnikovs, A. Glushkova, P. Matus, L. Ciric, M. Kollar, L. Forro, E. Horvath, A. Sienkiewicz, *ACS Photonics* **2018**, 5, 1476.
 [24] K.-C. Wang, J.-Y. Jeng, P.-S. Shen, Y.-C. Chang, E. W.-G. Diau, C.-H. Tsai, T.-Y. Chao, H.-C. Hsu, P.-Y. Lin, P. Chen, T.-F. Guo, T.-C. Wen, *Sci. Rep.* **2015**, 4, 4756.
 [25] Y. Wang, Y. Liang, Y. Zhang, W. Yang, L. Sun, D. Xu, *Adv. Funct. Mater.* **2018**, 28, 1801237.
 [26] D. Yang, R. Yang, K. Wang, C. Wu, X. Zhu, J. Feng, X. Ren, G. Fang, S. Priya, S. Liu, *Nat. Commun.* **2018**, 9, 3239.
 [27] X. Zhao, L. Tian, T. Liu, H. Liu, S. Wang, X. Li, O. Fenwick, S. Lei, W. Hu, *J. Mater. Chem. A* **2019**, 7, 1509.
 [28] M.-C. Wu, S.-H. Chan, K.-M. Lee, S.-H. Chen, M.-H. Jao, Y.-F. Chen, W.-F. Su, *J. Mater. Chem. A* **2018**, 6, 16920.
 [29] M.-C. Wu, S.-H. Chan, M.-H. Jao, W.-F. Su, *Sol. Energy Mater. Sol. Cells* **2016**, 157, 447.
 [30] T. Kotsoskechagia, F. Cellesi, A. Thomas, M. Niederberger, N. Tirelli, *Langmuir* **2008**, 24, 6988.
 [31] H. Tan, A. Jain, O. Voznyy, X. Lan, F. P. G. de Arquer, J. Z. Fan, R. Quintero-Bermudez, M. Yuan, B. Zhang, Y. Zhao, F. Fan, P. Li, L. N. Quan, Y. Zhao, Z.-H. Lu, Z. Yang, S. Hoogland, E. H. Sargent, *Science* **2017**, 355, 722.
 [32] K. J. Kubiak, M. C. T. Wilson, T. G. Mathia, P. Carval, *Wear* **2011**, 271, 523.
 [33] W.-Q. Wu, Z. Yang, P. N. Rudd, Y. Shao, X. Dai, H. Wei, J. Zhao, Y. Fang, Q. Wang, Y. Liu, Y. Deng, X. Xiao, Y. Feng, J. Huang, *Sci. Adv.* **2019**, 5, eaav8925.
 [34] X. Liu, Z. Liu, B. Sun, X. Tan, H. Ye, Y. Tu, T. Shi, Z. Tang, G. Liao, *Nano Energy* **2018**, 50, 201.
 [35] B.-X. Chen, H.-S. Rao, W.-G. Li, Y.-F. Xu, H.-Y. Chen, D.-B. Kuang, C.-Y. Su, *J. Mater. Chem. A* **2016**, 4, 5647.
 [36] X. Shi, Y. Ding, S. Zhou, B. Zhang, M. Cai, J. Yao, L. Hu, J. Wu, S. Dai, M. K. Nazeeruddin, *Adv. Sci.* **2019**, 6, 1901213.
 [37] S.-H. Chen, S.-H. Chan, Y.-T. Lin, M.-C. Wu, *Appl. Surf. Sci.* **2019**, 469, 18.
 [38] M. Vasilopoulou, N. Kelaidis, E. Polydorou, A. Soutlati, D. Davazoglou, P. Argitis, G. Papadimitropoulos, D. Tsikritzis, S. Kennou, F. Auras, D. G. Georgiadou, S.-R. G. Christopoulos, A. Chronos, *Sci. Rep.* **2017**, 7, 17839.

- [39] Q. Cui, X. Zhao, H. Lin, L. Yang, H. Chen, Y. Zhang, X. Li, *Nanoscale* **2017**, 9, 18897.
- [40] K.-C. Hsiao, M.-H. Jao, B.-T. Li, T.-H. Lin, S. H.-C. Liao, M.-C. Wu, W.-F. Su, *ACS Appl. Energy Mater.* **2019**, 2, 4821.
- [41] D. Ju, X. Jiang, H. Xiao, X. Chen, X. Hu, X. Tao, *J. Mater. Chem. A* **2018**, 6, 20753.
- [42] Y. Lin, B. Chen, Y. Fang, J. Zhao, C. Bao, Z. Yu, Y. Deng, P. N. Rudd, Y. Yan, Y. Yuan, J. Huang, *Nat. Commun.* **2018**, 9, 4981.
- [43] Y. Yuan, J. Huang, *Acc. Chem. Res.* **2016**, 49, 286.
- [44] R. Wang, M. Mujahid, Y. Duan, Z.-K. Wang, J. Xue, Y. Yang, *Adv. Funct. Mater.* **2019**, 29, 1808843.